

Supporting information for:

**Dynamics of the phospholipid shell of  
microbubbles: a fluorescence photoselection  
and spectral phasor approach**

Eli Slenders,<sup>a</sup> Senne Seneca,<sup>bc</sup> Sumit Kumar Pramanik,<sup>bc</sup> Nick Smisdom,<sup>a</sup>  
Peter Adriaensens,<sup>bc</sup> Martin vandeVen,<sup>a</sup> Anitha Ethirajan,<sup>bc‡</sup>  
and Marcel Ameloot<sup>a‡</sup>

<sup>a</sup> *Biomedical Research Institute (BIOMED), Hasselt University, Agoralaan Bldg. C, 3590 Diepenbeek, Belgium*

<sup>b</sup> *Institute for Materials Research (IMO), Hasselt University, Wetenschapspark 1 and Agoralaan Bldg. D, 3590 Diepenbeek, Belgium.*

<sup>c</sup> *IMEC, associated lab IMOMECE, Wetenschapspark 1, 3590 Diepenbeek, Belgium.*

<sup>‡</sup> *These authors contributed equally to this work.*

## Contents

<b>1 Laurdan fluorescence</b>	<b>3</b>
<b>2 Microbubble preparation</b>	<b>6</b>
<b>3 Microscopy imaging</b>	<b>8</b>
<b>4 GP analysis protocol</b>	<b>9</b>
<b>5 Dynamics of the microbubble shell structure</b>	<b>13</b>
<b>6 Shell phase separation</b>	<b>15</b>

## Summary

The Supporting Information provides detailed descriptions on the experimental methods employed, the analysis protocol used and the results obtained.

In the first section, the Laurdan molecule is described, and the fluorescence emission spectrum, as well as the principle of photoselection, is discussed. For reference purposes, a steady-state spectrum at 25 °C of Laurdan in dimethyl sulfoxide (DMSO) is provided, Fig. S3. Moreover, we provide an extension of the DMSO GP as a function of temperature, together with a unification of the use of instrument dependent GP correction factors as reported by others to alleviate confusion in the numerical values. We also present a convenient and sensitive GP based method to track the presence of water in the hygroscopic DMSO.

Next, section 2 provides details on the microbubble preparation protocol employing a two-step sonication method.

Section 3, *Microscopy imaging*, explains in detail the illumination and detection conditions of the laser scanning microscope set-ups.

In the fourth section, the generalized polarization (GP) analysis protocol is presented with the phasor approach for a compact and more intuitive comparison of resulting GP histograms.

The transition to a shell with high GP values and with the left-right photoselection may occur gradually, *i.e.* all parts of the shell will continuously increase in GP, without ever going through a distinct, spatially separated two-phase situation. A time series is presented in Fig. S9 to illustrate this behavior.

However, an alternative explanation is also discussed. Section 6 provides an example of a microbubble containing simultaneously the rigid and fluid-like phase. This data set shows that the transition towards the rigid phase may start locally, creating a time span in which both phases can exist.

## 1 Laurdan fluorescence

A schematic model of the fluorescent molecule Laurdan is shown in panel (a) of Fig. S1. The fluorescence spectrum is red-shifted in the presence of a polar environment, with the emission peak wavelength changing from 440 nm to 490 nm.<sup>1</sup> This property, together with the photoselection effect illustrated in panel (b), makes Laurdan suitable for probing the lipid organization in shells and membranes. The several models proposed for the T-B and the L-R photoselection effect are illustrated in Fig. S2.

Calibration of GP measurements with the microscopy setup is done by measuring the steady-

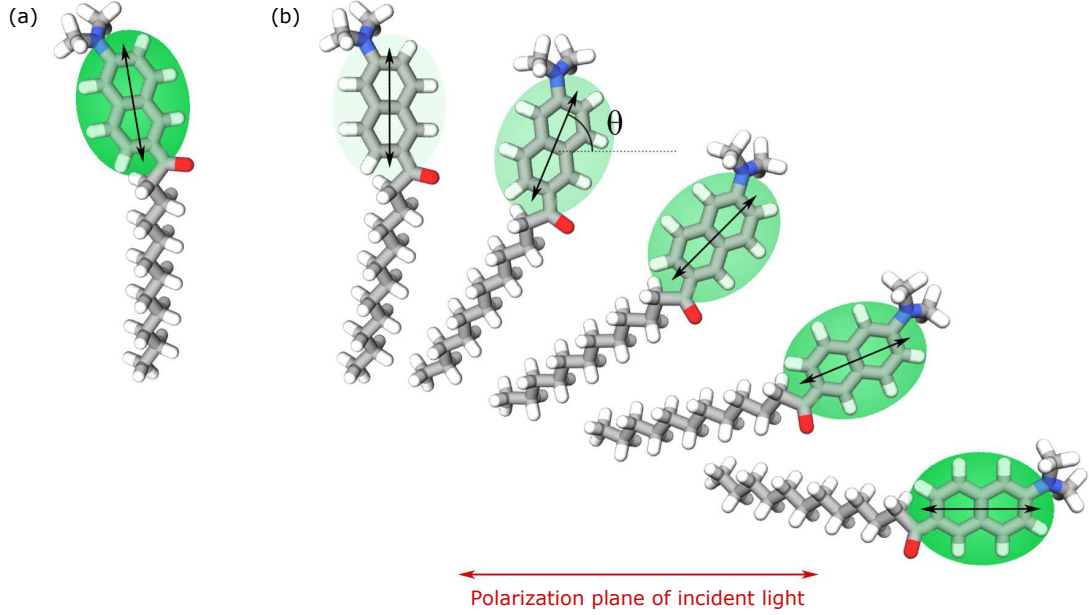


**Figure S1:** (a) Model of the Laurdan molecule. The green ellipse marks the naphthalene chromophore. The black arrow indicates the orientation of both the absorption and emission dipole moment.<sup>2,3</sup> The red and blue color represent respectively oxygen and nitrogen atoms. (b) The fluorescence intensity depends on the angle  $\theta$  between the Laurdan dipole moment and the polarization plane of the incident light, indicated by the red arrow. The photoselection effect follows a  $\cos^2 \theta$  relationship for 1-photon excitation and a  $\cos^4 \theta$  angular dependence for 2-photon excitation. The brightness of the green ellipse reflects the fluorescence intensity. The intensity distribution across the shell surface of a microbubble therefore provides information on the orientation of the chromophore.

state fluorescence spectrum of Laurdan in DMSO and comparing this reference result with the GP calculated in the two-channel microscopy setup using the same sample. Discrepancies caused by different sensitivities of the two detectors, the filter properties or any other optical effect are taken into account by computing a correction factor for the lipid measurements. The section *GP analysis protocol* further elaborates on this calculation.

Steady-state fluorescence spectra were obtained by an L-format Horiba Fluorolog Tau-3 photon counting spectrofluorimeter (Acal BFi, Eindhoven, The Netherlands). The temperature was controlled by a circulating refrigerated water bath (Neslab RTE-100, ThermoFisher-Scientific, Gent, Belgium) and, unless otherwise indicated, kept at 25 °C in a stoppered fused silica cuvette with internal miniature calibrated NTC temperature probe. Quinine sulphate system spectral sensitivity calibration was carried out according to the NIST protocol.<sup>4,5</sup> For Laurdan in DMSO, excitation was performed with a 450 W Xe arc lamp at 378 nm and the spectra were recorded in the range of 380 nm to 700 nm. The excitation and emission slit widths were 5 nm, the step size was 1 nm, the integration time was 1 s / step. The photon counting detector was operating in the linear response range. Spectra were blank corrected *i.e.* subtracting the contribution of DMSO without Laurdan. Each sample was measured at least

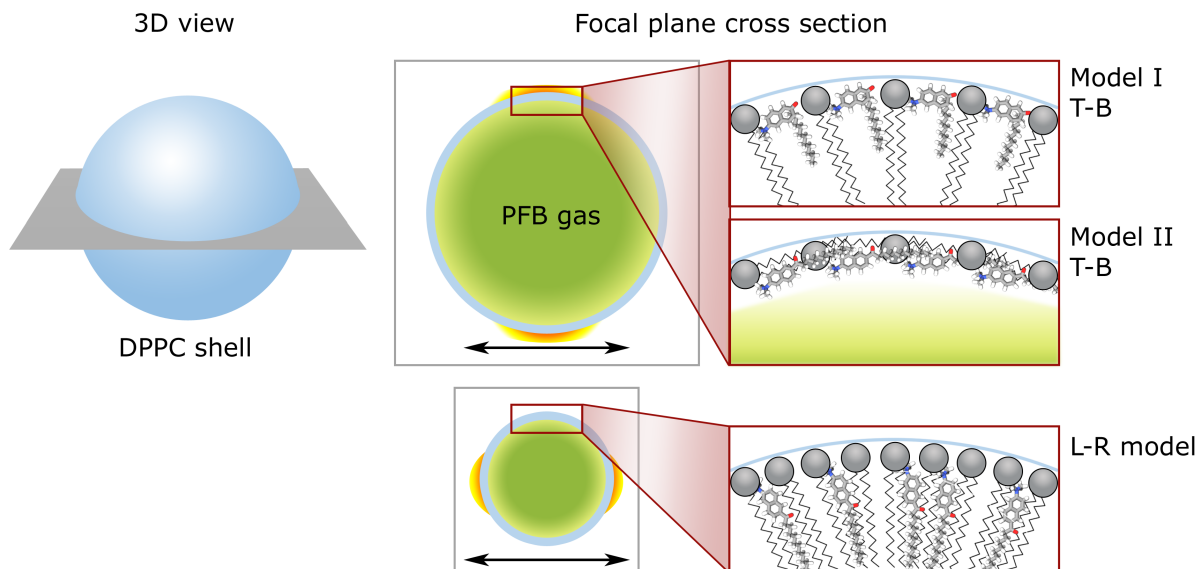


**Figure S2:** 3D view of a microbubble with the focal plane indicated. The cross section panels show in detail the proposed configurations for the Laurdan and DPPC molecules across the shell surface, both for a large microbubble with a T–B photoselection pattern and a smaller microbubble with an L–R fluorescence intensity pattern. The arrows indicate the polarization plane of the incident light. In model I and model II, the Laurdan chromophores are aligned with the shell surface and consequently the top and bottom part of the microbubble will produce the most intense fluorescence signal. In the smaller microbubble, the lipid density has increased, and therefore the lipid tails must be pointing radially, despite the lipophobicity of the PFB gas. Consequently, the Laurdan molecules will adopt the elongated shape and most of the fluorescence light will be produced by the left and right side of the bubble, see the L–R model.

in triplicate and averaged. Blank corrected concentrations were checked with similar settings and scan speed on a dual beam LS–45 spectrometer (Perkin Elmer, Waltham, MA, USA). The Laurdan fluorescence spectrum in DMSO is shown in Fig. S3.

### Additional remark on the Laurdan in DMSO calibration

Optical arrangement and emission path filter choice and specification as well as detector gain influences the instrument dependent  $\mathcal{G}$  correction factor for GP calculation. The factor is determined by measuring the GP of a Laurdan containing DMSO sample in the linear concentration dependent detection response range<sup>6</sup> and comparing this result with a reference value as measured with a steady–state spectrofluorimeter. Calibration samples must have been sufficiently temperature equilibrated and must have the same temperature as the samples under investigation. Illustrating the use of different microscope measurements and filter choice conditions, GP reference values of 0.006<sup>7</sup> and 0.207<sup>8</sup> can be found in the literature. A second concern of the calibration is the storage method and handling of the hygroscopic DMSO.

Therefore, we measured the temperature dependent reference GP as explained in the section

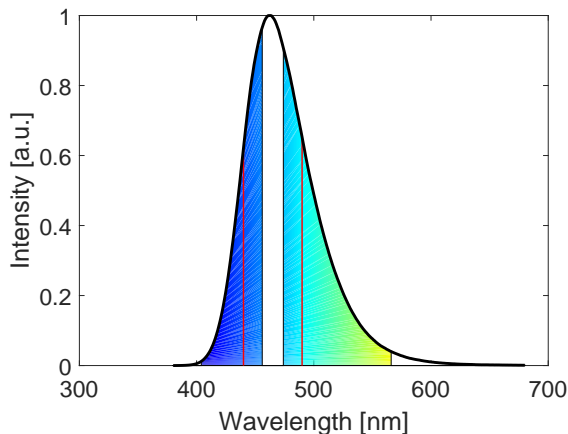


**Figure S3:** Corrected Laurdan fluorescence spectrum in DMSO at 25 °C. The colored regions correspond to the wavelength ranges of the blue and green channel filters of the microscopy setup. The red lines indicate 440 nm and 490 nm, used for the GP reference calculation, as explained in Section 4.

*Laurdan fluorescence*, resulting in the left panel of Fig. S4. Good agreement exists with Fig. S3 in Kaiser *et al.*<sup>9</sup> Upon further examination, the literature reference value of 0.207 could be understood assuming the use of rather old color glass filters with limited transmission and a sloping broad and partially overlapping spectral band pass.<sup>8,10–12</sup> Once steep cut-on optical interference based emission filters with a limited spectral bandwidth of  $(10 \pm 1)$  nm or  $(12 \pm 1)$  nm<sup>7,13</sup> became commercially available, instrument optical characteristics improved. The reported 0.006 value at room temperature for the correction factor was found to correspond with our photon counting spectrofluorimeter data within the tolerances as provided by the filter manufacturer.<sup>7</sup> Technological improvements have recently realized wider optical passband interference filters with a guaranteed transmission efficiency of 95 % or more.

Spiking the chromophore solution with small quantities of MilliQ water showed a visually nearly imperceptible red shift. However, as demonstrated in panel (b) of Fig. S4, the retrieved GP is highly influenced by the presence of small quantities of water.

## 2 Microbubble preparation

1,2-dipalmitoyl-*sn*-glycero-3-phosphocholine (DPPC) with a 16 carbon tail length was purchased from Avanti Polar Lipids (Alabaster, AL, USA). Spectroscopic grade chloroform (assay 99.3% stabilized with about 0.6% ethanol) was obtained from VWR (Haasrode, Belgium). HEPES buffer (pH 7.4) consisting of 10 mM HEPES from Alfa Aesar (assay 99%) and 150 mM NaCl from Sigma Aldrich (assay > 99.5%) was used to hydrate the lipid film. Perfluorobutane (PFB) gas was obtained from F2 Chemical Ltd (Lea Lane, Lea Town, UK). Laurdan (6-Dodecanoyl-N,N-dimethyl-2-naphtylamine) and dimethyl sulfoxide anhydrous (DMSO) (>

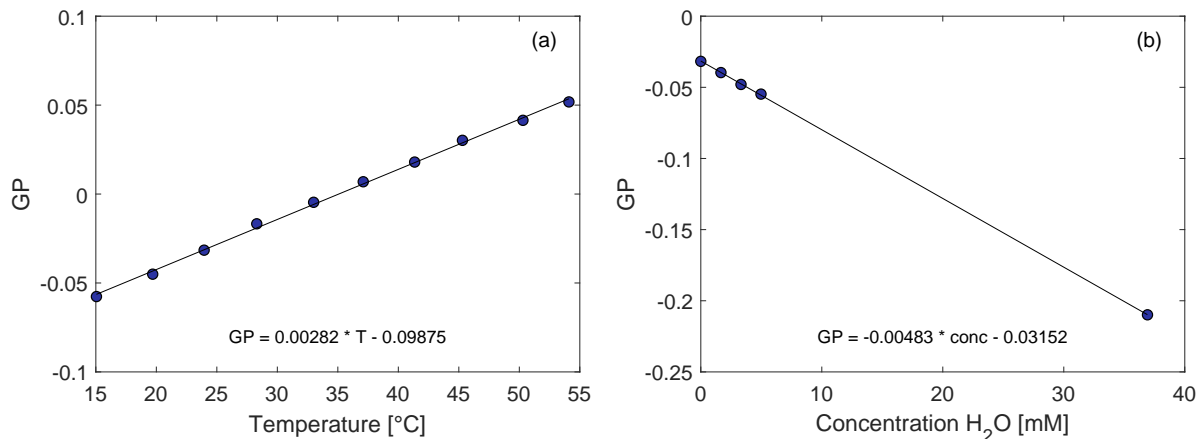


**Figure S4:** (a) Laurdan in DMSO calibration for various temperatures. (b) Laurdan in DMSO calibration at 25 °C for various amounts of water added. Small quantities of water present in the hygroscopic DMSO significantly influence the obtained correction factor.

99.9%) were purchased from Sigma Aldrich (Diegem, Belgium). DMSO was kept in the dark under vacuum before use, handled in a dry nitrogen gas filled glove box and was regularly spectroscopically checked using Laurdan for any presence of water. Deionized water obtained from a Sartorius Stedim biotech machine was used throughout the experiments.

For the microbubble preparation, in order to avoid debris (unwanted lipid aggregates), a two-step sonication method was developed: in the first step, indirect sonication (using Cup Horn sonicator 450 W digital sonifier, Branson, Danbury, USA) was applied to generate larger PFC-filled microbubbles in a closed vial enclosing the formulation. Subsequently, in the second step, using direct sonication (probe sonicator 450 W digital sonifier, Branson, Danbury, USA) the larger microbubbles ( $> 50 \mu m$ ) were broken down into smaller ones ( $< 50 \mu m$ ) in an open vial.

Briefly, the formulation protocol used was the following: DPPC lipid was first dissolved in chloroform (10 mg/mL) in a scintillation vial, blown dry with a mild flow of nitrogen (2 bar) in a closed vial, and further dried overnight under vacuum. The lipid film was then hydrated to 5 mM with HEPES buffer, swirled and sonicated at 60 Hz in a VWR ultrasonic cleaner for 120 s at room temperature (21 °C) to detach the lipid, as well as to promote its dispersion. Next, the vial was incubated for 90 min in an oven (Binder, Model BD 56, Tuttlingen, Germany) at sufficiently high temperature - around 20 °C above the main phase transition temperature of DPPC ( $T_{m,DPPC} = 41.4 \text{ } ^\circ\text{C}$ ). Thereafter, a mild stream (1 bar) of PFB gas (F2 Chemicals Ltd, Preston, UK) was applied for 150 s, followed by indirect sonication in a closed vial using the Cup Horn sonicator (employing an amplitude of 70 %) for 90 s ensuring the efficient encapsulation of PFB gas in larger microbubbles. Then, the larger microbubbles were broken down into smaller ones ( $< 50 \mu m$ ) in an open vial by the probe sonicator employing a  $\frac{1}{4}$ " tip and an amplitude

of 35 % for 30 *s*. The sonication frequency of the cup horn sonicator and the probe sonicator is 20 *kHz*. Finally, the Laurdan (0.5 *mM* solution in DMSO) was added to the microbubble sample in a 1:500 molar ratio and incubated for 30 *min* at room temperature.

All microbubble samples were washed before imaging or spectroscopic measurements to remove excess probe and debris. To this extent, the microbubble solution was diluted with buffer solution (5x), shaken for a few seconds, and centrifuged for 2 *min* (using the refrigerated centrifuge Sigma 3–30K and rotor number 12154H) at 300 *rpm* (RCF = 8 g). Subsequently, the preparation was left for settling for around 3 *min* during which the floatation of microbubbles on top of the solution occurred. This procedure was repeated three times. After each centrifugation step, the supernatant was removed and fresh HEPES buffer (pH 7.4) was added to the microbubble sample. Afterwards, the preparations were immediately inspected with respect to microbubble morphology, dispersity, and colloidal stability using an Axiovert 40 MAT optical microscope (Carl Zeiss, Oberkochen, Germany). Clean preparations were stored in the dark and at 4 °C until further use.

### 3 Microscopy imaging

Microscopy images were obtained with a Zeiss LSM510 META (Carl Zeiss Microscopy GmbH, Jena, Germany) confocal microscope system mounted on an inverted Axiovert 200 M. Unless mentioned otherwise, imaging was performed with a 40x/1.1 water immersion objective (LD C-Apochromat 40x/1.1 W Korr UV-VIS-IR, Carl Zeiss).

7  $\mu\text{L}$  of the sample suspension was poured in a spacer (Grace Bio-Labs SecureSeal imaging spacer, diameter 9 *mm*, height 0.12 *mm*) mounted on a microscope slide. A cover slip (thickness #1.5) was pressed onto the spacer. The complete assembly was positioned on the thermostated microscope stage. Measurements were collected on temperature equilibrated samples. Due to the large diameter, most microbubbles were lying still during the acquisition time of an image, which took typically about 15 *s*. If the microbubble had moved during acquisition, another image was taken. For the long time series measurement, refocusing during the imaging process was necessary to correct for axial drift.

Two photon excitation (2PE) was performed with a femtosecond pulsed laser (Mai Tai DeepSee, Spectra-Physics Inc., Santa Clara, CA, USA) tuned to a central wavelength of 780 *nm*. Incident laser power at the sample was kept sufficiently low to avoid heating effects or other imaging-induced artifacts such as photobleaching. For photoselection measurements with a rotating excitation polarization plane, LSM510 emission signals were detected with an analog photomultiplier tube in non-descanned, transmission mode after passing through a condenser

lens, a 470 *nm* beam splitter and a bandpass filter *BP475 – 565 nm*. The sample temperature was controlled using a cage incubator built around the microscope stage and a temperature controller (Tempcontrol 37-2 digital, PeCon GmbH, Erbach, Germany). Mechanical stability of the microscope setup was ensured by prior incubator warmup. Temperature at the sample position was checked with a calibrated NTC sensor.

A home built polarization device containing a rotatable half wave and quarter wave plate was installed under the objective. The orientation of the half wave plate was automatically adjusted with stepper motors (Trinamic PD-110-42, Hamburg, Germany) before the start of each image scan to make a series of images with different orientations of the linearly polarized illuminating laser light see Fig. S5.

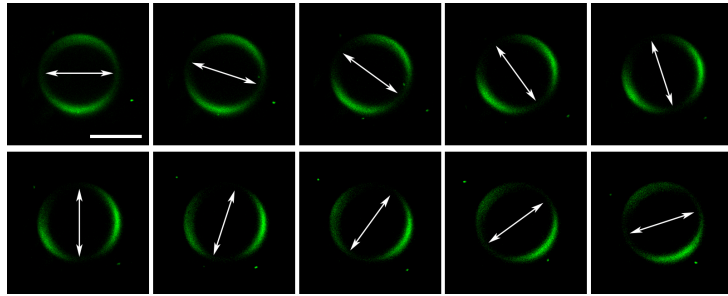


**Figure S5:** Excitation polarization dependence of the fluorescence of Laurdan in the equatorial plane of a DPPC-PFB microbubble at 25 °C. White arrows indicate the plane of excitation polarization which is varied in steps of 18 °. Emission bandpass filter 475 – 565 *nm*. Zeiss Plan-Apochromate 20x/0.75 objective. The scale bar in the upper left image represents 50  $\mu\text{m}$ .

For GP imaging, Fig. S6, the polarization device was exchanged for a short pass 725 *nm* dichroic beam splitter under the objective to measure the signal in backward mode. The emission signal was split by a 470 *nm* beam splitter and detected with two analog photomultiplier tubes. As indicated in Fig. S3, *BP405 – 455 nm* and *BP475 – 565 nm* emission bandpass filters were used for the blue and the green channels respectively. Simultaneously, the transmission signal was detected in forward mode after passing through a condenser lens.

## 4 GP analysis protocol

The generalized polarization (GP) is defined as<sup>1,14-20</sup>

$$GP = \frac{I_B - I_R}{I_B + I_R}, \quad (1)$$

where  $I_B$  and  $I_R$  are the fluorescence intensity at 440 *nm* and 490 *nm* respectively. Limiting values are +1 (highest GP) and -1 (lowest GP). High GP values in a lipid environment correspond to a rigid, ordered shell phase. Low GP values indicate a more fluid, disordered phase.

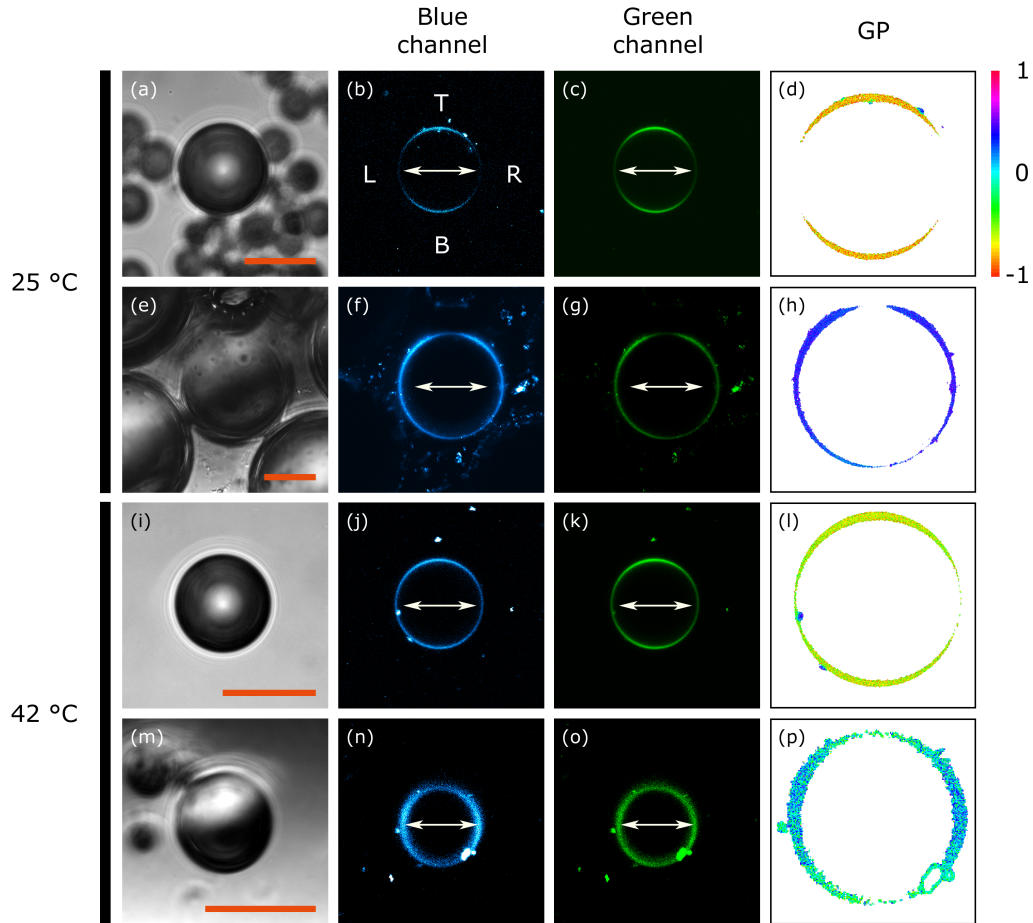


**Figure S6:** Photoselection and Generalized Polarization (GP) observed in Laurdan stained DPPC-PFB microbubbles imaged with 2PE laser scanning microscopy. From left to right, column 1 (a, e, i, m): transmission images. Column 2 (b, f, j, n): blue Laurdan fluorescence emission channel (BP 405 – 455 nm). Column 3 (c, g, k, o): green Laurdan fluorescence emission channel (BP 475 – 565 nm). Right column (d, h, l, p): GP calculated pixel wise from the blue and green images. Most transmission images show multiple microbubbles. However, because of the optical sectioning effect intrinsically present in 2PE fluorescence microscopy, only the sections of the microbubbles that are in focus are clearly visible in the blue and green fluorescence channels. Top and third row images show bright top (T) and bottom (B) shell regions, while the left (L) and right (R) side emit less fluorescence. The apparent shell thickness is influenced by the photoselection effect, creating the illusion of thicker TB shell segments compared to the L and R sides, top row. The second and fourth row exhibit an opposite pattern. GP values are indicated by the upper right color bar. The excitation polarization is horizontal, as indicated by the white arrows. Illumination wavelength is 780 nm. Scale bars are 50  $\mu\text{m}$  and hold for the first three columns. The microbubbles in the GP panels are set to the same diameter. Brightness and contrast are individually adjusted for all images for visualization purposes.

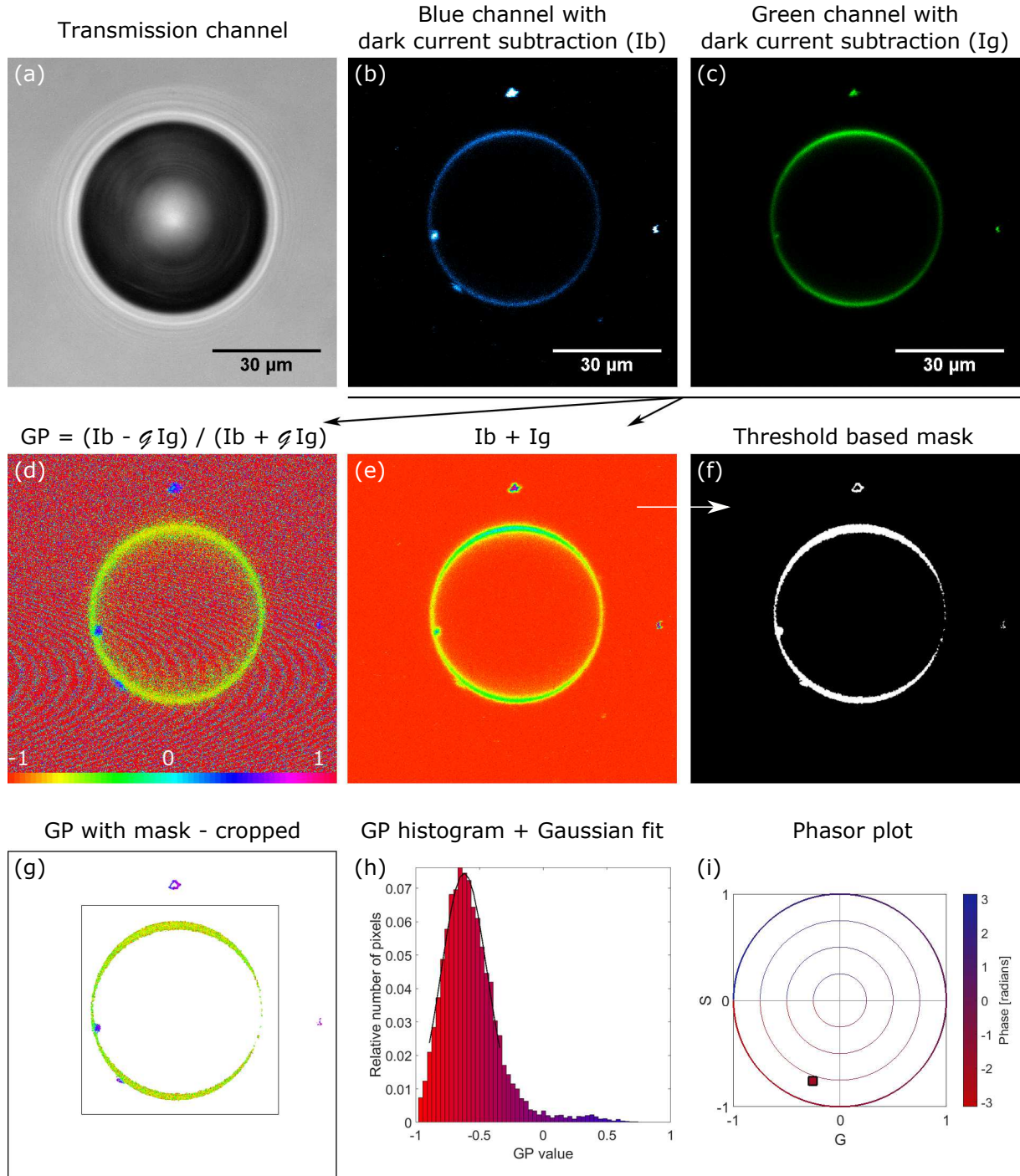


**Figure S7:** Generalized Polarization (GP) analysis protocol illustrated with a DPPC-PFB microbubble at 42 °C.

Each step in the GP protocol is illustrated by a panel of Fig. S7. Analysis of the acquired microscopy data was performed with in-house developed Matlab scripts (Matlab R2017b, The Mathworks, Inc., Eindhoven, The Netherlands).

First, microbubble microscopy images in the transmission, blue and green channels are shown in panels (a)–(c). The dark current signal was subtracted from each pixel value. From both images, the GP was calculated pixel wise, panel (d), using the formula

$$GP = \frac{I_B - \mathcal{G}I_R}{I_B + \mathcal{G}I_R}, \quad (2)$$

with  $I_B$  and  $I_R$  the fluorescence intensity, *i.e.* the pixel value, in the blue (405-455 nm) and green (475-565 nm) channel, respectively. The parameter  $\mathcal{G}$  is a correction factor<sup>7</sup> used to calibrate the instrumental spectral response, since the absolute GP value is strongly affected by instrument specific factors. This  $\mathcal{G}$  factor also compensates for the effect of using band pass filters instead of measuring at single peak wavelengths.<sup>21</sup>

Calibration experiments were performed by comparing microscopy images of Laurdan in the reference solution DMSO with steady-state fluorescence spectra of the same sample recorded on a thermostated Fluorolog Tau-3 photon counting spectrofluorimeter. Applying Eq. 1 to the measured spectrum at room temperature (21 °C) yields a GP value of Laurdan in DMSO of 0.068. The  $\mathcal{G}$  factor for the microscopy setup is then calculated by plugging in this reference value in the following formula:

$$\mathcal{G} = \frac{I_B(1 - GP)}{I_R(1 + GP)}. \quad (3)$$

$I_B$  and  $I_R$  are the average intensity values measured with the fluorescence microscope in the blue and green channel, respectively.

For optimal signal-to-background, the sum of the fluorescence signal in the blue and the green channel, panel (e), was used to create a mask, panel (f), by setting pixel values above a user defined threshold to 1 and background pixels to 0. A smoother mask was created by a median filter. This filter was then applied to the GP image, panel (g), removing the background signal from the microbubble shell.

A histogram of the remaining GP values was calculated, panel (h). Instead of solely evaluating the peak location by fitting the top of the histogram with a Gaussian function, as shown with the black line, we used the phasor calculation.<sup>20,22</sup> This method does not only analyze the histogram peak, but instead, all bins are taken into account. The result is a single point in Fourier space, panel (i).

Phasor calculation produces a coordinate set  $(G, S)$  in two dimensions by applying the following transformation:

$$G = \frac{\sum \#(GP) \cos(2\pi n GP/L)}{\sum \#(GP)}, \quad (4)$$

$$S = \frac{\sum \#(GP) \sin(2\pi n GP/L)}{\sum \#(GP)}, \quad (5)$$

where  $\#(GP)$  is the bin height in the histogram with center value GP,  $n$  is the number of the harmonic, set to 1 for the first order phasor used here, and  $L$  is the difference between the maximum and minimum GP value possible, *i.e.* 2. Summation runs over all GP bins.

The presented protocol is a novel way for mapping the shell structure of lipid microbubbles. Instead of calculating the phasor coordinates based on a complete spectrum<sup>20,22–24</sup>, our implementation only requires the measurement of the fluorescence intensity based image in two optical channels. The shape of the resulting GP histogram obtained over the monolayer related pixels is analyzed with the phasor calculation. The phasor approach is appealing since it is a model-free transformation that produces a single coordinate in Fourier space. Interpretation of the data and comparison of several conditions becomes convenient and intuitive. Data points located in the lower left quadrant of the phasor plot correspond to the least rigid and most water molecule accessible shell structure. By rotating counterclockwise, one enters regions with a higher and more ordered shell structure and reduced access of water molecules to the chromophore. The width of the GP distribution can be derived from the distance to the origin; the higher the modulus ( $S^2 + G^2$ ), *i.e.* the distance from the center, the narrower the GP distribution.<sup>18</sup> The phasor approach is used in Fig. S8 to compare the shell rigidity of 21 individual microbubbles. GP values cluster in two regions. A majority of the microbubbles has a low, negative GP, at room temperature and at 42 °C. A small fraction has a positive GP. A single microbubble was imaged during its transition from the former to the latter group.

## 5 Dynamics of the microbubble shell structure

We measured the temporal evolution of the shell rigidity of a single microbubble in a time series experiment, shown in Fig. S9. In a time span of several hours, the microbubble drastically changes from a low GP shell structure with a top-bottom photoselection towards a high GP structure with a left-right selection. During this process, the microbubble shrinks about 35 % in diameter, see Fig. S10 (a), which corresponds to a reduction in the surface area of about 58 %. It can be concluded from panel (b) of Fig. S10 that the transition is accompanied by large

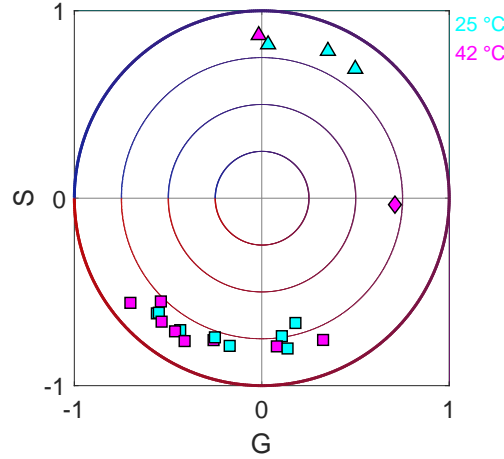


**Figure S8:** Phasor plot of 11 DPPC–PFB microbubbles at 25 °C and 10 microbubbles at 42 °C. Three classes of microbubbles can be found using a hierarchical cluster algorithm in Matlab. The first class, class I, represented by the squares, corresponds to lipid shells with negative GP values and a top–bottom photoselection effect. Shell structures that became more rigid after the shrinking process constitute a second group, class II, with much higher GP values, indicated by the positions of the triangular data points, and a left–right fluorescence intensity pattern under horizontally polarized laser light. The diamond shape (center right) refers to a microbubble in a third group, class III, undergoing the transition from the first to the second class during the shrinking process. The lower left quadrant of the plots corresponds to a low overall GP, close to  $-1$ , as indicated by the red colored circle segments. Data points located counterclockwise from this quadrant have continuously increasing GP values up to  $+1$  in the upper left quadrant, as illustrated with the color gradient in the circles. The larger the distance from the center of the circle, the narrower the GP distribution.

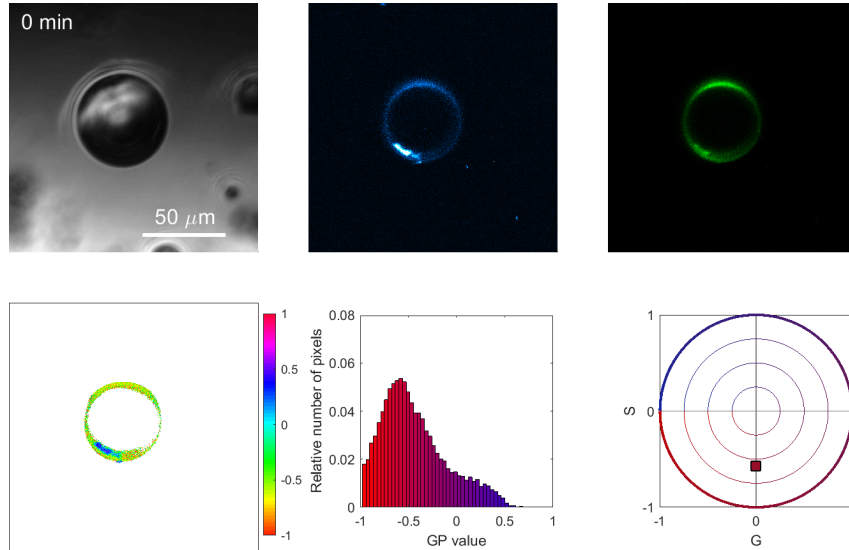


**Figure S9:** First frame of a time series video (*Fig\_S9\_time\_series.mp4*) showing the transition from a low GP lipid monolayer to a more rigid, high GP shell structure during the shrinking process. Top row: transmission channel, blue fluorescence channel and green fluorescence channel respectively. Bottom row: pixelwise calculated GP, GP histogram and phasor plot respectively. Between minutes 120 and 180, the bubble moves partially away from the focal plane. The effect is much more conspicuous in the fluorescence channels compared to the transmission images due to the optical sectioning effect in two–photon fluorescence microscopy as compared with Mie scattering effects. The sample was refocused several times during acquisition to account for this axial drifting. No significant lateral movement, nor tumbling, was observed.

fluctuations in the fluorescence intensity. Shedding sections visible at a given image scan have disappeared in the next scan 2 minutes later. These ubiquitous shedding shell sections display a high GP and may be related to reported zippering effects resulting in bilayer structures.<sup>25–30</sup> Shedding events disappeared during the final hour of observations, Fig. S10 (b). The stability of the resulting rigid shell structure can be derived not only from the high GP values, but also from the very stable fluorescence intensity starting 4 hours after the beginning of the measurement. Simultaneously collected transmission images show a persistent gas fill since the imaged circumference water–gas interface displays for the length of the recording a black rim due to refraction at the interface.

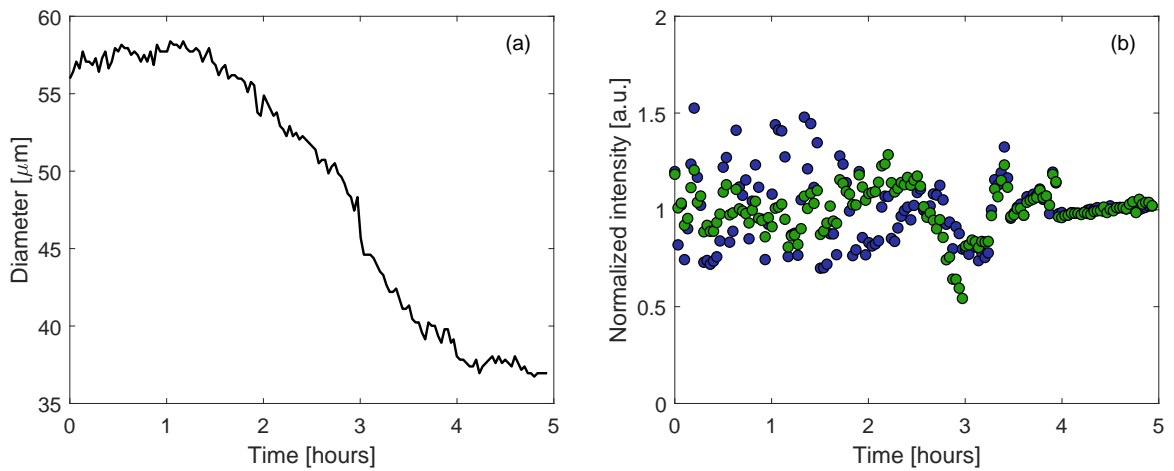


**Figure S10:** (a) Microbubble diameter as a function of time for the shrinking microbubble in Fig. S9 and Fig. 2 (main text), measured by manually selecting the white microbubble border in each frame of the transmission channel. (b) Corresponding fluorescence intensity in the blue and green channel, normalized to the average intensity per pixel for the first time point.

## 6 Shell phase separation

Even though most microbubbles show a top–bottom angular dependence with low GP values or a left–right selection with high GP values, we also imaged a microbubble with a clear spatial phase separation, see Fig. S11. The left side of the microbubble has a positive GP, indicating a local rigid domain in an otherwise negative GP shell. This image shows that the transition towards a rigid shell structure can start locally, and does not need to happen in all sections of the bubble simultaneously. It cannot be excluded, however, that this peculiar arrangement resulted from a merger of two neighboring microbubbles. **Enhanced resolution microscopy techniques, such as structured illumination microscopy<sup>31</sup> and single molecule techniques<sup>32,33</sup>, may be helpful as a future guideline to check the effect of possible dye clustering on the observed**

GP values. This requires that proper laser excitation is available for the Laurdan dyes and that probe concentrations are validated for absence or presence of concentration quenching. This observation resembling Ostwald type ripening seems to be a very rare event.

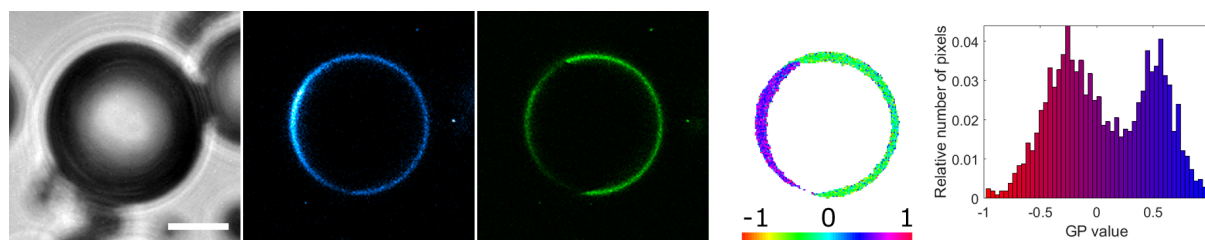


**Figure S11:** From left to right: transmission image, blue fluorescence channel, green fluorescence channel, GP image and GP histogram of a DPPC–PFB microbubble at 42 °C showing phase separation. The scale bar represents 20  $\mu\text{m}$ .

## References

- (1) T. Parasassi, G. De Stasio, A. Dubaldo and E. Gratton, *Biophys. J.*, 1990, **57**, 1179–1186.
- (2) S. Osella, N. A. Murugan, N. K. Jena and S. Knippenberg, *J. Chem. Theory Comput.*, 2016, **12**, 6169–6181.
- (3) M. Bacalum, L. N. Wang, S. Boodts, P. J. Yuan, V. Leen, N. Smisdom, E. Fron, S. Knippenberg, G. Fabre, P. Trouillas, D. Beljonne, W. Dehaen, N. Boens and M. Ameloot, *Langmuir*, 2016, **32**, 3495–3505.
- (4) R. A. Velapoldi and K. D. Mielenz, *Appl. Optics*, 1981, **20**, 1718–1718.
- (5) D. Pfeifer, K. Hoffmann, A. Hoffmann, C. Monte and U. Resch-Genger, *J. Fluoresc.*, 2006, **16**, 581–7.
- (6) J. R. Lakowicz, *Principles of Fluorescence Spectroscopy*, Springer, 3rd edn., 2011.
- (7) J. Brewer, J. B. de la Serna, K. Wagner and L. A. Bagatolli, *BBA-Biomembranes*, 2010, **1798**, 1301–1308.
- (8) K. Gaus, T. Zech and T. Harder, *Mol. Membr. Biol.*, 2006, **23**, 41–48.
- (9) H. J. Kaiser, D. Lingwood, I. Levental, J. L. Sampaio, L. Kalvodova, L. Rajendran and K. Simons, *P. Natl. Acad. Sci. USA*, 2009, **106**, 16645–16650.
- (10) S. A. Sanchez, M. A. Tricerri and E. Gratton, *P. Natl. Acad. Sci. USA*, 2012, **109**, 7314–9.
- (11) D. M. Owen, D. J. Williamson, A. Magenau and K. Gaus, *Nat. Commun.*, 2012, **3**, 1256.
- (12) I. P. Sousa, C. A. M. Carvalho, D. F. Ferreira, G. Weissmuller, G. M. Rocha, J. L. Silva and A. M. O. Gomes, *J. Biol. Chem.*, 2011, **286**, 1730–1736.
- (13) J. S. Hansen and C. Helix-Nielsen, *Biochem. Biophys. Res. Co.*, 2011, **415**, 686–90.
- (14) T. Parasassi and E. Gratton, *J. Fluoresc.*, 1995, **5**, 59–69.
- (15) T. Parasassi, E. Gratton, W. M. Yu, P. Wilson and M. Levi, *Biophys. J.*, 1997, **72**, 2413–2429.
- (16) L. A. Bagatolli and E. Gratton, *Biophys. J.*, 1999, **77**, 2090–2101.
- (17) L. A. Bagatolli and E. Gratton, *J. Fluoresc.*, 2001, **11**, 141–160.
- (18) E. Sezgin, D. Waithe, J. B. de la Serna and C. Eggeling, *Chem. Phys. Chem.*, 2015, **16**, 1387–1394.

- 
- (19) M. Aron, R. Browning, D. Carugo, E. Sezgin, J. B. de la Serna, C. Eggeling and E. Stride, *BMC Bioinformatics*, 2017, **18**, 8.
- (20) L. Malacrida, E. Gratton and D. M. Jameson, *Methods Appl. Fluores.*, 2015, **3**, 047001.
- (21) T. Parasassi, G. De Stasio, G. Ravagnan, R. M. Rusch and E. Gratton, *Biophys. J.*, 1991, **60**, 179–189.
- (22) O. Golfetto, E. Hinde and E. Gratton, *Methods Mol. Biol.*, 2015, **1232**, 273–90.
- (23) M. Stefl, N. G. James, J. A. Ross and D. M. Jameson, *Analytical Biochemistry*, 2011, **410**, 62–69.
- (24) F. Fereidouni, A. N. Bader and H. C. Gerritsen, *Opt. Express*, 2012, **20**, 12729–12741.
- (25) M. A. Borden and M. L. Longo, *Langmuir*, 2002, **18**, 9225–9233.
- (26) M. A. Borden, D. E. Kruse, C. F. Caskey, S. K. Zhao, P. A. Dayton and K. W. Ferrara, *IEEE T. Ultrason. Ferr.*, 2005, **52**, 1992–2002.
- (27) S. Baoukina, L. Monticelli, H. J. Risselada, S. J. Marrink and D. P. Tieleman, *P. Natl. Acad. Sci. USA*, 2008, **105**, 10803–10808.
- (28) M. L. Longo, M. M. Lozano and M. A. Borden, *Bubble Sci. Eng. Technol.*, 2009, **1**, 18–30.
- (29) J. J. Kwan and M. A. Borden, *Adv. Colloid Interfac.*, 2012, **183**, 82–99.
- (30) M. A. Borden, *Curr. Opin. Colloid In.*, 2014, **19**, 480–489.
- (31) C. E. Schutt, S. D. Ibsen, M. J. Benchimol, M. J. Hsu and S. C. Esener, *Small*, 2014, **10**, 3316–3324.
- (32) Y. Liu, J. A. Feshitan, M. Y. Wei, M. A. Borden and B. H. Yuan, *J. Biomed. Opt.*, 2015, **20**, 8.
- (33) Q. M. Zhang, S. P. Morgan and M. L. Mather, *Small*, 2017, **13**, 12.